nature geoscience

ARTICLES

https://doi.org/10.1038/s41561-020-0575-4



# Widespread subsidence and carbon emissions across Southeast Asian peatlands

Alison M. Hoyt[1,4]✉, Estelle Chaussard[2], Sandra S. Seppalainen[1] and Charles F. Harvey[1,3]

**Over the last three decades, most of the 25 million hectares of tropical peatlands in Southeast Asia have been deforested and drained. As a consequence, declining water tables are exposing peat to oxidation, converting plant material accumulated over millennia to carbon dioxide, and causing land subsidence. Here, we quantify the widespread peat carbon loss by using InSAR remote sensing to map subsidence at 90-m resolution across 2.7 Mha of peatland area from 2007 to 2011. Over 90% of the surveyed area is subsiding, with a mean rate of 2.2 cm yr$^{-1}$. Consequently, the region now faces loss of productive land and flooding because many peatlands are near sea level. Our measurements reveal that smallholder agricultural areas and degraded peatlands are subsiding at rates comparable to those of plantations, and that subsidence rates increase away from rivers and decrease over time following drainage. Because of its detailed spatial resolution, InSAR provides a valuable tool to identify emissions by land use and geography and to target hotspots for better management. Finally, we use remotely sensed maps to update IPCC emissions factors and calculate regional $CO_2$ emissions from peat oxidation of 155 ± 30 MtC yr$^{-1}$ in 2015, similar in magnitude to both regional fossil-fuel emissions and peat fires.**

The estimated 25 Mha of peatlands in Southeast Asia remained as relatively undisturbed freshwater peat swamp forests before the 1980s. By 2015 only 6% of the area remained as pristine peatland[1]. In Insular Southeast Asia, most peatlands have been converted to industrial plantations (27%), smallholder agriculture (22%) or degraded peat swamp forests (23%)[1]. The drainage accompanying this land conversion lowers the water table, exposing peat soil to oxygen, allowing aerobic oxidation and fire, and resulting in $CO_2$ emissions and subsidence of the peatland surface[2]. The large organic carbon stock within tropical peat (66–69 Gt)[3] is being emitted as $CO_2$ at a rate of 132–159 MtC yr$^{-1}$ in 2015, estimated on the basis of IPCC (Intergovernmental Panel on Climate Change) emissions factors[4].

Most studies have used poles anchored into the underlying clay[2,5–12] to document subsidence of tropical peatlands. They observed initial rates of subsidence up to 75 cm yr$^{-1}$ from compaction after drainage, followed by long-term subsidence rates up to 5 cm yr$^{-1}$ from oxidation and loss of peat to $CO_2$ emissions[2]. If these rates persist, many coastal tropical peatlands that are only a few metres above sea level will experience frequent flooding or complete inundation and saltwater intrusion in the coming decades[13].

These studies are limited by the low number of poles, the challenges of multiyear monitoring and the inaccessibility of field sites. They have primarily focused on oil palm plantations, neglecting land uses such as smallholder farming. Media reports and industry groups have leveraged this data gap to cast doubt on whether subsidence is widespread or long lasting[14]. While the mechanisms linking subsidence to peatland drainage are well established[15], the spatial extent and trajectory over time remains controversial.

In this work, we present a large-scale high-resolution assessment of subsidence on tropical peatlands. We use Interferometric Synthetic Aperture Radar (InSAR) remote sensing to monitor subsidence in tropical peatlands across Southeast Asia, covering 2.7 Mha, or over 10% of the region's peatland area. We systematically document subsidence across all disturbed land-use categories, including smallholder agriculture, shrubs, ferns, cleared/burnt areas and degraded forests. Over 90% of the peatland area surveyed is subsiding, demonstrating that subsidence is not limited to plantations.

## InSAR remote sensing of subsidence

Our InSAR remote sensing approach characterizes subsidence at 90-m resolution across 4.3 Mha in Southeast Asia, including 2.7 Mha of tropical peatlands. InSAR is an active remote sensing technique, which detects centimetre- to millimetre-scale changes in elevation by measuring phase changes in the reflected microwave beam between subsequent flyovers of a SAR spacecraft (every 46 d for the Advanced Land Observing Satellite—ALOS)[16]. Subsidence rates are derived by taking the linear fit to the time series of deformation at each pixel (Fig. 1). This approach has been used to quantify volcanic deformation, earthquakes and interseismic deformation, and to manage aquifer systems[16–21]. Recently, subsidence due to peatland drainage in the Netherlands and Wales[22,23], local subsidence associated with the construction of Kuala Lumpur International Airport on tropical peatland[24] and subsidence on drained and restored peatlands in Jambi and Central Kalimantan, Indonesia[25], was quantified using InSAR. Our large-scale InSAR analysis expands on these previous datasets to cover all major land-use classes on tropical peatlands.

We measure subsidence across eight 100 × 100 km$^2$ frames in Indonesia and Malaysia (Fig. 2a, Extended Data Table 1, Extended Data Figs. 6–9 and Supplementary Figs. 1–4) using a correlation-based selection method[18,26] derived from the Small Baseline Subset time-series approach[27], relying on ALOS L-band data from 2007–2011. We filter out regional deformation, such as the Sumatra subduction zone, and compare our subsidence maps with established maps of peatland extent and historical land use developed by Miettinen et al.[1] to analyse spatial and temporal trends (Methods).

We demonstrate that the correlation-based InSAR time-series method applied to L-band data overcomes several obstacles to

[1]Department of Civil and Environmental Engineering, Massachusetts Institute of Technology, Cambridge, MA, USA. [2]Department of Earth Sciences, University of Oregon, Eugene, OR, USA. [3]Center for Environmental Sensing and Modeling, Singapore–MIT Alliance for Research and Technology, Singapore, Singapore. [4]Present address: Max Planck Institute for Biogeochemistry, Jena, Germany. ✉e-mail: ahoyt@bgc-jena.mpg.de

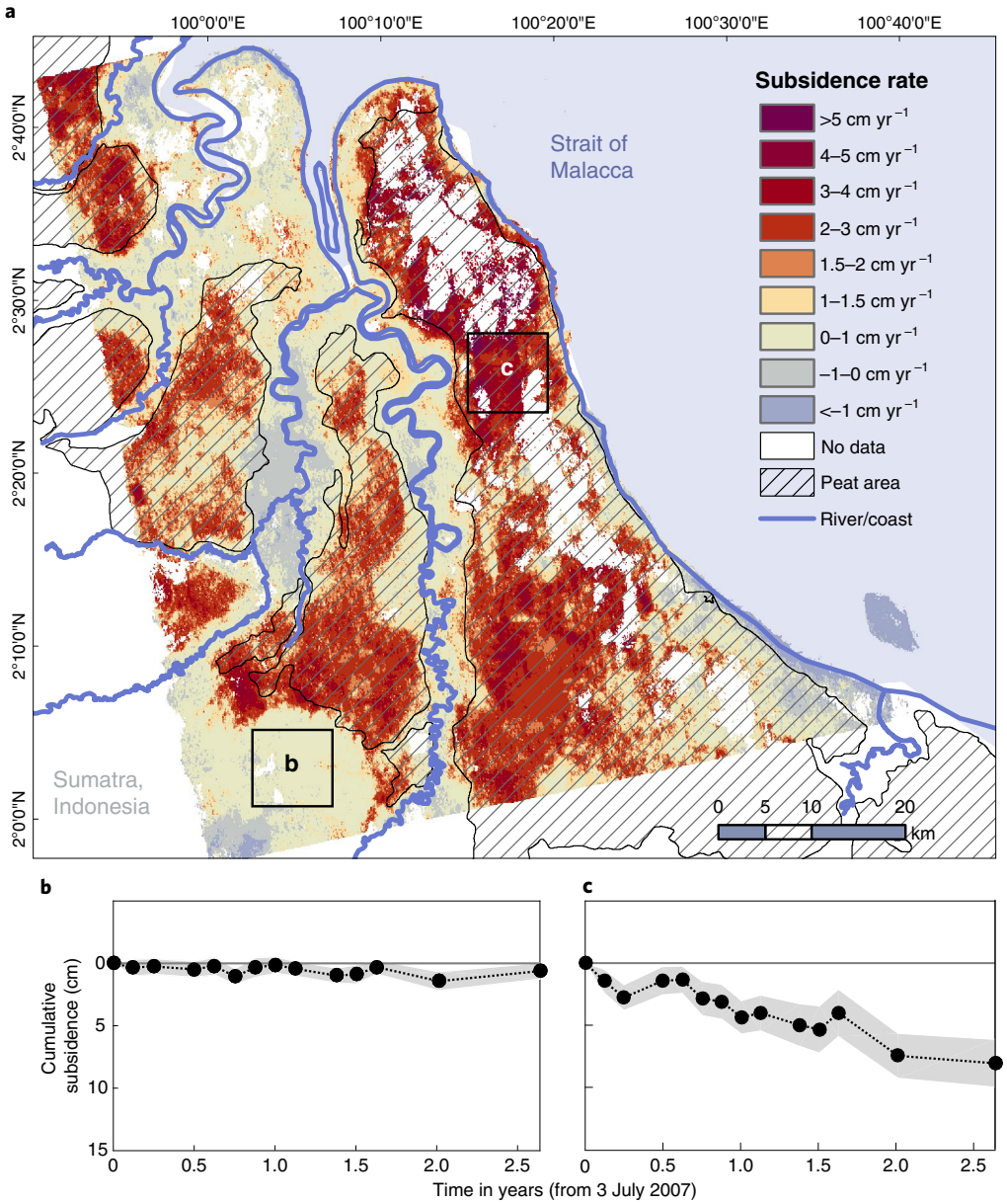


**Fig. 1 | Subsidence rates and time series in peat and non-peatland areas in ALOS frame 1 of 8.** (For other frames analysed, see Fig. 2a, Extended Data Figs. 6–9 and Supplementary Figs. 1–4.) **a**, Map of subsidence rates across coastal peatlands in North Sumatra and Riau provinces, Sumatra, Indonesia. Highest subsidence rates are found within irregularly shaped peatlands (hashed, peatland extent reproduced with permission from from ref. [1], Elsevier). **b**, Time series of cumulative subsidence in the indicated non-peatland area show negligible change in the land surface elevation. **c**, Time series of cumulative subsidence in the indicated peatland area (s.d. in grey). Positive values indicate subsidence and negative values indicate uplift.

measuring long-term subsidence in drained tropical peatlands: penetration of dense vegetation, maintaining signal coherence through time and avoiding phase-unwrapping errors. First, in contrast to previous approaches with C-band data[22–24], L-band data enable some canopy penetration and maintain coherence in oil palm plantations and areas with partially open canopy such as small-scale agriculture, shrubland, burned areas and degraded peat swamp forests[25]. Second, measurements of long-term subsidence due to peat carbon loss, which are the focus of this study, are minimally impacted by signal decorrelation or phase-unwrapping errors. Decorrelation is expected if a substantial change in the land surface or canopy texture occurs within the 46-d return period, and phase-unwrapping errors occur when the deformation between repeat passes is greater than half the ALOS wavelength (24 cm). These processes are expected with rapid subsidence due to short-term compaction immediately following deforestation or with large fires[2], but long-term subsidence due to peat oxidation is of the order of 1–5 cm $yr^{-1}$ (0.13–0.63 cm per 46 d), minimizing decorrelation and unwrapping errors. Furthermore, fires are almost entirely excluded from our analysis because of the low fire frequency during our study period (Supplementary Fig. 8 and Supplementary Table 2). Our analysis is therefore well suited to measuring subsidence from peat oxidation because initial compaction and fires are excluded.

We validate the estimated subsidence rates from InSAR time series and mean velocity maps in several ways. First, we confirm that subsidence maps show no deformation in non-peatland areas and show clear and accurate delineation of the subsiding peat boundaries (Figs. 1 and 2). These areas provide an estimate

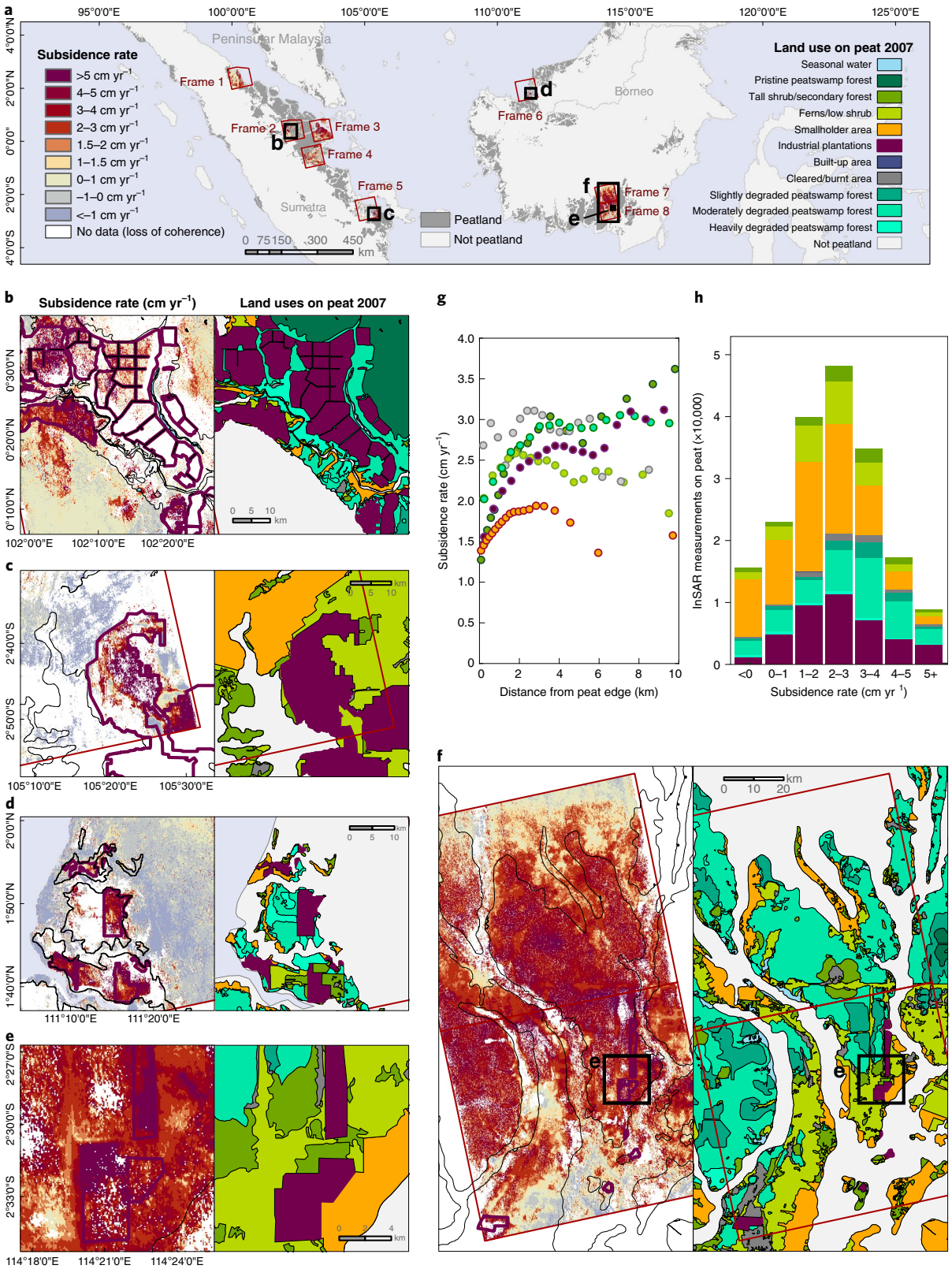


**Fig. 2 | Subsidence and land-use maps. a**, Study area in Southeast Asia (peatland areas in grey[1]), including eight ALOS frames analysed (outlined in red), and insets (outlined in black). **b**–**f**, Details of subsidence rate maps at different spatial scales (left-hand panels; left-hand legend in **a**) alongside their corresponding land-use maps from ref. [1] (right-hand panel; right-hand legend). Boundaries of peatland areas (black line) and industrial plantations (purple lines) overlay the InSAR subsidence rates. Locations are ALOS frame 2 (**b**), frame 5 (**c**), frame 6 (**d**), frame 8 (**e**) and frames 7 and 8 (**f**). ALOS frame 1 is shown in Fig. 1. **g**, Binned subsidence versus distance from the edge of the peat (20 bins) for 0–10 km (slightly, moderately and heavily degraded peatlands shown together). **h**, Histogram of mean subsidence rates across all InSAR pixels on peatland. Positive values indicate subsidence and negative values indicate uplift. Peatland extent and land-use maps adapted with permission from ref. [1], Elsevier.

**Table 1 | Land use, InSAR subsidence rates, and ground-based studies**

| Land use | Land area in 2015 (%) | InSAR-measured subsidence (cm yr$^{-1}$) (mean ± s.d.) | Bootstrapped subsidence (upscaling) (cm yr$^{-1}$) (mean ± s.e.m.) | Regional emissions factor (upscaling) (tC ha$^{-1}$ yr$^{-1}$) | Ground-based subsidence studies | Number of subsidence poles | Number of InSAR pixels |
|---|---|---|---|---|---|---|---|
| Industrial plantation | 27.4 | 2.6 ± 1.7 | 2.5 ± 0.2 | 11.0 ± 2.0 | DID & LAWOO[6]<br>Wösten et al.[11]<br>Maswar[30]<br>Othman et al.[8]<br>Hooijer et al.[2]<br>Couwenberg & Hooijer[9]<br>Ishikura et al.[29]<br>Evans et al.[5] | 22 (2 sites; oil palm (OP))<br>17 (1 site; OP)<br>5 (1 site; OP)<br>25 (5 sites; OP)<br>125 (1 site; acacia)<br>51 (2 sites; OP)<br>1 (1 site; OP)<br>220 (acacia) | 414,718 |
| Degraded peat swamp forest | 22.8 | 2.8 ± 1.7 | 2.5 ± 0.6 | 11.2 ± 3.1 | Nagano et al.[10]<br>Ritzema et al.[12]<br>Khasanah & van Noordwijk[28] | 4 (1 site)<br>19 (4 sites)<br>12 (1 site) | 440,756 |
| Smallholder area | 22.4 | 1.7 ± 1.6 | 1.8 ± 0.3 | 7.7 ± 1.9 | Taylor & Ali[7]<br>Khasanah & van Noordwijk[28] | 20 (2 sites)<br>44 (4 sites) | 673,915 |
| Tall shrub/secondary forest | 11.1 | 2.6 ± 1.7 | 2.4 ± 0.3 | 10.4 ± 2.2 | - | - | 89,929 |
| Ferns/low shrub | 5.4 | 2.2 ± 1.4 | 2.2 ± 0.2 | 9.6 ± 1.8 | - | - | 215,439 |
| Cleared/burnt area | 2.0 | 2.8 ± 1.5 | 2.5 ± 0.2 | 11.2 ± 2.1 | - | - | 41,800 |
| Urban area | 0.3 | 1.0 ± 0.2 | - | - | - | - | 166 |

Subsidence rates for each land cover class are calculated from both InSAR measurements and bootstrapped regression-tree-based regional upscaling. Emissions factors are calculated from bootstrapped subsidence values. We find similar subsidence rates across land uses. We exclude peatland areas classified as pristine (6.5%), seasonal water (1.7%), mangrove (0.4%) or water (0.3%), as the InSAR coverage was poor and these areas are not expected to experience subsidence. Data were insufficient to calculate an emissions factor for urban areas on peat (0.3%). The fraction of peatland area is reported from ref. [1].

of the method's accuracy and precision with an overall measured mean subsidence of 0.21 cm yr$^{-1}$, and an s.d. of 1.05 cm yr$^{-1}$, in non-peatland areas >15 km from the peat edge (Extended Data Figs. 1 and 2 and Supplementary Table 3). However, due to the lack of direct ground-based validation, it is possible that the s.d. is higher for peatlands. Second, we verify that spatial discontinuities in subsidence rates correspond to past or present land-use boundaries in nearly all cases (Fig. 2). Finally, we validate trends in InSAR subsidence rates with subsidence pole measurements across land-use categories (Extended Data Fig. 4)[2,5–12,28,29]. Point-by-point comparison is not possible due to limited ground measurements between 2007 and 2011[2,8], a lack of precise coordinates for monitoring poles, and subpixel heterogeneity within the 90-m SAR resolution (Methods).

## Subsidence trends across Southeast Asian peatlands

We find widespread subsidence across Southeast Asian peatlands, regardless of land use. Over 90% of the peat is subsiding, with approximately 80% subsiding at rates > 1 cm yr$^{-1}$, 60% at rates > 2 cm yr$^{-1}$ and 15% at rates > 4 cm yr$^{-1}$ (Fig. 2h). These rates are consistent with ground-based measurements (Extended Data Fig. 4), but are now observed across large areas and diverse land uses.

Our remote sensing analysis shows that subsidence extends beyond plantations, with comparable mean subsidence rates across distinct land-use categories (Table 1). Degraded peatlands and smallholder areas cover 23% and 22% of regional peatland area respectively, but account for only a small number of pole measurements[10,12,28] (Table 1), as most studies have focused on plantations[2,5,6,8,9,11,29,30]. While previous upscaling efforts assumed, for example, that plantations subside over five times faster than degraded peat swamp forests[4], or twice as fast as smallholder agriculture and three times faster than shrublands and recently cleared/burnt areas[31], our large-scale analysis reveals comparable mean subsidence rates across land uses. This enables important updates to IPCC emissions factors and confirms that the drainage itself, rather than land use, is the principal driver of the subsidence.

Although subsidence is observed across all land-use categories, rates are not uniform across the landscape or within land-use categories. In many cases, land-use boundaries are clearly reflected in subsidence patterns, probably due to different drainage depths in adjacent areas (Fig. 2c,e). However, in other regions, such as the Ex-Mega-Rice project area, subsidence is consistent across the landscape despite differences in land use, probably due to systematic drainage efforts (Fig. 2f). Regional peat properties such as peat depth, degree of decomposition and mineral content may also contribute to variability in subsidence rates (Extended Data Fig. 2). Subsidence rates may also be influenced by warming temperatures resulting from climate and land-use change[32–34].

Subsidence rates are higher further from rivers and peat margins, independent of land-use history (Figs. 1a, 2g and 3c) and across land-use categories. This finding is consistent with understanding[31,35] of the interaction between peat morphology and hydrology: the water table within a peat dome cannot fall below the water level of its bounding rivers, hence subsidence is limited at the dome margins, where the peat is thinnest. Subsidence is greater in dome interiors, where drainage can expose thick layers of peat to oxidation. We note that at the largest distances from the river the subsidence rates appear to once again decrease; however, this signal is dominated by a few locations. This large-scale pattern of increasing subsidence with distance from rivers contrasts with the small-scale pattern of decreasing subsidence with distance from canals[11]. Near canals, the largest water table drawdowns are immediately adjacent to the bank, causing the highest subsidence. In the future, detailed

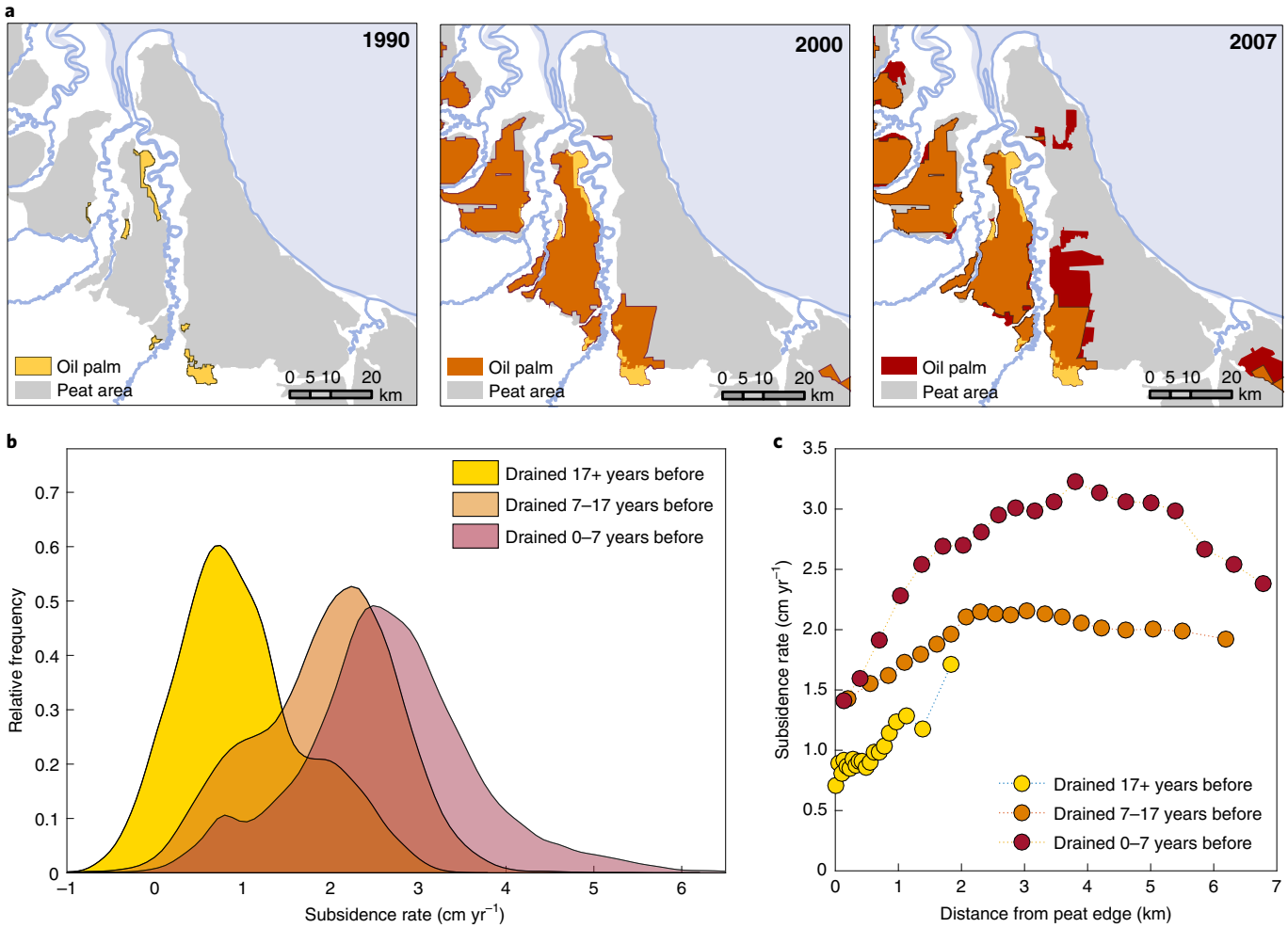


**Fig. 3 | Subsidence rates over time since oil palm plantation establishment. a**, Expansion of oil palm plantations on peatland from 1990 to 2007 across coastal areas in North Sumatra and Riau, Sumatra, Indonesia (ALOS frame 1, see Fig. 1 for subsidence rates and geographic coordinates). **b**, Probability density estimate of InSAR subsidence rates on oil palm plantations at different stages of development. **c**, Subsidence rates binned by distance from the river (20 bins). Subsidence rates are higher on recently drained plantations, and show an increase in subsidence away from the river. 0–7-yr data are limited to points <7 km from the peat boundary for consistency with 7–17-yr data. Peatland extent and land-use maps in **a** adapted with permission from ref. [1], Elsevier.

subsidence maps may help to design canal systems to better manage subsidence.

This subsidence dataset also allows us to address a question of regional importance: does subsidence slow over time? Long-term subsidence rates as high as 5 cm yr$^{-1}$ have been observed in ground-based measurements[2]. If maintained, these rates could result in flooding within a few decades. In contrast, other pole measurements have shown that subsidence slows over time[8,11]. To address this question, we use a space-for-time substitution approach. We compare subsidence rates in adjacent peatland areas in North Sumatra that were drained and converted to oil palm plantations at different times (Fig. 3a). Subsidence rates on recently established plantations are the highest and decrease with time since conversion (Fig. 3b), even when accounting for distance from the river (Fig. 3c). Potential causes for slowed subsidence with time include the following: (1) a change in peat properties if preferential decomposition of labile organic matter leaves behind a more stable peat matrix; (2) drainage depths could decrease over time if canals are not maintained; (3) in some cases, all peat may have decomposed, exposing the underlying mineral soil and lowering average rates for old plantations. Longer-term trends in subsidence rates (beyond 20 yr) remain uncertain.

## Upscaling subsidence to carbon losses

Subsidence measurements, when combined with bulk density data, integrate carbon loss over time and capture all carbon fluxes from the peat (including for example fluvial C export[36]). The increase in subsidence measurements from hundreds of poles to hundreds of thousands of InSAR measurements (Table 1) enables us to extrapolate subsidence values and corresponding $CO_2$ emissions across insular Southeast Asia, on the basis of extensive spatial coverage. This represents an improvement over existing regional studies, which calculated regional $CO_2$ emissions from peat oxidation by multiplying a single emissions factor by the total area in each land-use category[4,31], sometimes relying on a handful of data points for large areas.

Across all pixels, we find a mean regional subsidence of 2.24 cm yr$^{-1}$ (Supplementary Table 1). To upscale these measurements across the region, beyond the eight InSAR frames, while still accounting for differences in the regional land-use distribution (Supplementary Fig. 7), we use a regression-tree approach based on (1) classification of present land use at the time of subsidence measurements, (2) distance from the peat edge and (3) past land use (1990) as a proxy for time since drainage (Extended Data Fig. 3). Using a bootstrapping approach to generate 1,000 regression

trees, we find a similar upscaled mean regional subsidence rate of $2.24 \pm 0.23$ cm yr$^{-1}$ (mean ± s.e.m.; Methods, Supplementary Table 1 and Supplementary Fig. 6). Because the variability in site-specific drainage practices is high, it is challenging to accurately predict subsidence at a single location, which is reflected by the large s.d. in measured subsidence values (Table 1). In contrast, across the region, this variability averages out, reducing the uncertainty in the regional mean subsidence. To estimate regional $CO_2$ emissions due to peat oxidation, we multiply the subsidence rate by the peat bulk density and carbon content, following the method of Couwenberg and Hooijer[9] and using values and uncertainty ranges for peat properties from the literature (Methods and Extended Data Fig. 5).

We find that drainage of tropical peatlands in insular Southeast Asia resulted in a net carbon loss of $155 \pm 30$ MtC yr$^{-1}$ in 2015, confirming that long-term peat oxidation is a large source of $CO_2$ emissions, consistent with previous regional estimates[4,31]. As our upscaling does not consider Indonesian Papua and Papua New Guinea, home to an additional ~10 Mha of tropical peatlands, which are poorly mapped, our results probably underestimate the total $CO_2$ emissions from peat oxidation in Southeast Asia. Wider application of InSAR is needed to further identify subsidence hotspots and inform regional management practices.

## Online content

Any methods, additional references, Nature Research reporting summaries, source data, extended data, supplementary information, acknowledgements, peer review information; details of author contributions and competing interests; and statements of data and code availability are available at https://doi.org/10.1038/s41561-020-0575-4.

Received: 30 April 2019; Accepted: 6 April 2020;
Published online: 04 June 2020

## References

1. Miettinen, J., Shi, C. & Liew, S. C. Land cover distribution in the peatlands of Peninsular Malaysia, Sumatra and Borneo in 2015 with changes since 1990. *Glob. Ecol. Conserv.* **6**, 67–78 (2016).
2. Hooijer, A. et al. Subsidence and carbon loss in drained tropical peatlands. *Biogeosciences* **9**, 1053–1071 (2012).
3. Page, S. E., Rieley, J. O. & Banks, C. J. Global and regional importance of the tropical peatland carbon pool. *Glob. Change Biol.* **17**, 798–818 (2011).
4. Miettinen, J., Hooijer, A., Vernimmen, R., Liew, S. C. & Page, S. E. From carbon sink to carbon source: extensive peat oxidation in insular Southeast Asia since 1990. *Environ. Res. Lett.* **12**, 024014 (2017).
5. Evans, C. D. et al. Rates and spatial variability of peat subsidence in *Acacia* plantation and forest landscapes in Sumatra, Indonesia. *Geoderma* **338**, 410–421 (2019).
6. *Western Johore Integrated Agricultural Development Project, Peat Soil Management Study* (Department of Irrigation and Drainage (DID), Kuala Lumpur, Malaysia and Land and Water Research Group (LAWOO), 1996).
7. Taylor, D. & Ali, M. *Biogeochemical Responses to Land Cover Changes in Coastal Peatland Catchments: Spatial and Temporal Fluxes in Greenhouse Gas Emissions and Peat Subsidence, Jambi Province, Sumatra* (SARCS/UNOP, 2001).
8. Othman, H., Mohammed, A. T., Darus, F. M., Harun, M. H. & Zambri, M. P. Best management practices for oil palm cultivation peat: ground water-table maintenance in relation to peat subsidence and estimation of $CO_2$ emissions at Sessang, Sarawak. *J. Oil Palm Res.* **23**, 1078–1086 (2011).
9. Couwenberg, J. & Hooijer, A. Towards robust subsidence-based soil carbon emission factors for peat soils in south-east Asia, with special reference to oil palm plantations. *Mires Peat* **12**, 1 (2013).
10. Nagano, T. et al. Subsidence and soil $CO_2$ efflux in tropical peatland in southern Thailand under various water table and management conditions. *Mires Peat* **11**, 6 (2013).
11. Wösten, J., Ismail, A. & van Wijk, A. Peat subsidence and its practical implications: a case study in Malaysia. *Geoderma* **78**, 25–36 (1997).
12. Ritzema, H., Limin, S., Kusin, K., Jauhiainen, J. & Wösten, H. Canal blocking strategies for hydrological restoration of degraded tropical peatlands in Central Kalimantan, Indonesia. *Catena* **114**, 11–20 (2014).
13. Whittle, A. & Gallego-Sala, A. V. Vulnerability of the peatland carbon sink to sea-level rise. *Sci. Rep.* **6**, 28758 (2016).
14. Wijedasa, L. S. et al. Denial of long-term issues with agriculture on tropical peatlands will have devastating consequences. *Glob. Change Biol.* **23**, 977–982 (2017).
15. Carlson, K. M., Goodman, L. K. & May-Tobin, C. C. Modeling relationships between water table depth and peat soil carbon loss in Southeast Asian plantations. *Environ. Res. Lett.* **10**, 074006 (2015).
16. Bürgmann, R., Rosen, P. A. & Fielding, E. J. Synthetic aperture radar interferometry to measure Earth's surface topography and its deformation. *Annu. Rev. Earth Planet. Sci.* **28**, 169–209 (2000).
17. Chaussard, E., Amelung, F., Abidin, H. & Hong, S.-H. Sinking cities in Indonesia: ALOS PALSAR detects rapid subsidence due to groundwater and gas extraction. *Remote Sens. Environ.* **128**, 150–161 (2013).
18. Chaussard, E. et al. Interseismic coupling and refined earthquake potential on the Hayward-Calaveras fault zone. *J. Geophys. Res. Solid Earth* **120**, 8570–8590 (2015).
19. Massonnet, D. et al. The displacement field of the Landers earthquake mapped by radar interferometry. *Nature* **364**, 138–142 (1993).
20. Fialko, Y. Interseismic strain accumulation and the earthquake potential on the southern San Andreas fault system. *Nature* **441**, 968–971 (2006).
21. Pritchard, M. E. & Simons, M. An InSAR-based survey of volcanic deformation in the southern Andes. *Geochem. Geophys. Geosyst.* **5**, L15610 (2004).
22. Cuenca, M. C. & Hanssen, R. Subsidence due to peat decomposition in the Netherlands: kinematic observations from radar interferometry. In *Fifth International Workshop on ERS/Envisat SAR Interferometry, 'FRINGE07'* 1–6 (2008).
23. Cigna, F., Sowter, A., Jordan, C. J. & Rawlins, B. G. Intermittent Small Baseline Subset (ISBAS) monitoring of land covers unfavourable for conventional C-band InSAR: proof-of-concept for peatland environments in North Wales, UK. *Proc. SPIE* **9243**, 924305 (2014).
24. Marshall, C. et al. Monitoring tropical peat related settlement using ISBAS InSAR, Kuala Lumpur International Airport (KLIA). *Eng. Geol.* **244**, 57–65 (2018).
25. Zhou, Z. *The Applications of InSAR Time Series Analysis for Monitoring Long-Term Surface Change in Peatlands*. PhD thesis, Univ. Glasgow (2013).
26. Chaussard, E. et al. Potential for larger earthquakes in the East San Francisco Bay Area due to the direct connection between the Hayward and Calaveras Faults. *Geophys. Res. Lett.* **42**, 2734–2741 (2015).
27. Berardino, P., Fornaro, G., Lanari, R. & Sansosti, E. A new algorithm for surface deformation monitoring based on small baseline differential SAR interferograms. *IEEE Trans. Geosci. Remote Sens.* **40**, 2375–2383 (2002).
28. Khasanah, N. & van Noordwijk, M. Subsidence and carbon dioxide emissions in a smallholder peatland mosaic in Sumatra, Indonesia. *Mitig. Adapt. Strateg. Glob. Change* **24**, 147–163 (2019).
29. Ishikura, K. et al. Soil carbon dioxide emissions due to oxidative peat decomposition in an oil palm plantation on tropical peat. *Agric. Ecosyst. Environ.* **254**, 202–212 (2018).
30. Maswar, M. *Kajian Cadangan Karbon pada Lahan Gambut Tropika Yang Didrainase Untuk Tanaman Tahunan* (*Carbon Stock in the Drained Tropical Peat Used for Perennial Plantation Crops*). PhD dissertation, Bogor Agricultural Univ. (2011).
31. Hooijer, A. et al. Current and future $CO_2$ emissions from drained peatlands in Southeast Asia. *Biogeosciences* **7**, 1505–1514 (2010).
32. Hirano, T., Jauhiainen, J., Inoue, T. & Takahashi, H. Controls on the carbon balance of tropical peatlands. *Ecosystems* **12**, 873–887 (2009).
33. Jauhiainen, J., Kerojoki, O., Silvennoinen, H., Limin, S. & Vasander, H. Heterotrophic respiration in drained tropical peat is greatly affected by temperature—a passive ecosystem cooling experiment. *Environ. Res. Lett.* **9**, 105013 (2014).
34. Hoyt, A. M. et al. $CO_2$ emissions from an undrained tropical peatland: interacting influences of temperature, shading and water table depth. *Glob. Change Biol.* **25**, 2885–2899 (2019).
35. Cobb, A. R. et al. How temporal patterns in rainfall determine the geomorphology and carbon fluxes of tropical peatlands. *Proc. Natl Acad. Sci. USA* **114**, E5187–E5196 (2017).
36. Moore, S. et al. Deep instability of deforested tropical peatlands revealed by fluvial organic carbon fluxes. *Nature* **493**, 660–663 (2013).

## Methods

**Site selection.** Sites were selected to cover representative land uses on peat across Southeast Asia, including agricultural plantations, smallholder areas and degraded peat swamp forest. The spatial scale of ALOS frames ($100 \times 100\,km^2$) results in a mix of land uses in each frame (Extended Data Table 1). Preference was given to sites where concurrent subsidence pole measurements are available, such as frame 6, which includes the region with the measurements of Othman et al.[8]. Frame 9 includes the oil palm measurements by Hooijer et al.[2] and Couwenberg and Hooijer[9], but a two-year gap in the ALOS time series prevented further analysis. Frame 2 overlaps with acacia plantation, where measurements by Hooijer et al.[2] were made, but decorrelation occurs in the localized area of the pole measurements, probably due to dense forest cover.

**InSAR data processing.** We employed InSAR, the best technology currently available for dense spatial sampling of ground deformation at local to national scales. InSAR measures ground displacement in the radar line-of-sight (LOS) direction of a SAR satellite between different passes of the satellite over the same area[16]. We used data from ALOS of the Japanese Space Exploration Agency. The long wavelength (L-band, 24 cm) of the radar system on board the ALOS satellite enables deformation monitoring even in highly vegetated areas such as Indonesia[25,37], in contrast with previous works relying on C-band data[22–24]. Although suitable for temperate peatlands, the shorter-wavelength C-band signal is poorly adapted to the dense vegetation and high subsidence rates found in tropical peatlands[24]. ALOS acquired data with global coverage between late 2006 and mid-2011 on a 46-d repeat orbit, imaging most of the world's continents 25 times or more[37] with data freely available through the Alaska Satellite Facility.

We used the ISCE (InSAR Scientific Computing Environment) software to produce interferograms, removed topographic contributions using the Shuttle Radar Topography Mission 1-arcsec digital elevation model, coregistered all interferograms of each frame to a master image and used the statistical-cost network-flow algorithm for phase unwrapping (SNAPHU)[38]. To precisely track ground deformation between the first and the last SAR acquisition we used a correlation-based time-series technique[18,26] derived from the Small Baseline Subset method[27]. Both methods combine many interferograms and invert them to retrieve the surface displacement through time, but the correlation-based selection method relies on using only interferograms with high coherence in a selected area of interest[18,26] (Supplementary Figs. 9 and 11). The correlation-based method ensures higher coherence in the resulting mean velocity map even in vegetated or cultivated areas[18,26], and limits bias from soil moisture change since interferograms between distinct seasons (wet and dry) affected by a decrease in coherence are not included (Supplementary Figs. 9 and 10). We multilooked the data three times (90-m pixel) to increase the coherence and reduce the computing time. The processing scheme includes removal of topography-correlated atmospheric noise[39] and removal of long-wavelength signals in the form of a quadratic ramp to decrease orbital artifacts and ionospheric noise and eliminate potential interseismic or postseismic contributions from the Sumatra subduction zone[40]. Errors correlated with elevation and baselines (digital elevation model errors) were removed following the method of Fattahi and Amelung[41], and unwrapping errors were identified using the phase closure technique and manually corrected.

InSAR analysis provides a time series of the observed signal at each pixel that maintains similar ground characteristics between successive passes (temporal coherence >0.4), and a mean velocity map showing the average speed at which the ground is moving in the LOS of the satellite (Fig. 1b,c and Supplementary Fig. 5). Time series were first screened for outliers and then used to calculate the mean linear subsidence rates. Uncertainties in the InSAR time series were evaluated following the method of Chaussard et al.[42], in which the temporal variability of the signal at pixels in non-deforming areas is considered to evaluate the time-dependent background noise level and identify acquisitions affected by strong ionospheric and tropospheric noise or remaining small unwrapping errors. Soil moisture variations were considered to result in minimal noise[43–45], as we applied a digital elevation model error correction, removed unwrapping errors, relied on linear averages in which the nonlinear signal (such as the soil moisture component) is part of the noise and used a correlation-based method with temporal coherence masking (Supplementary Figs. 9 and 10).

Ionospheric noise is related to the total electron content of the upper atmosphere and its impact is about 16 times greater for L-band than C-band SAR data due to the frequency dependency of the ionosphere refractive index. Ionospheric noise results in a long-wavelength signal across an interferogram. In contrast, tropospheric delays result from changes in the refractive index due to variations in atmospheric pressure, temperature and water vapour in the lower atmosphere. Tropospheric noise is more spatially localized than ionospheric noise, does not affect an entire SAR frame and correlates with topography. Both ionospheric and tropospheric noise are temporally random. Outlier dates in the time series associated with ionospheric or tropospheric noise were identified on the basis of the background noise level mentioned above (Extended Data Table 1) and were removed without influencing preceding or following acquisitions, as all measurements were referenced to the first SAR date. Residual atmospheric noise contributes to our uncertainty estimates. Unwrapping errors occur when the change in land surface elevation is misinterpreted by half a wavelength (12 cm), which was infrequent in our case as typical subsidence rates are 1–5 cm $yr^{-1}$ (0.13–0.63 cm per 46 d). In time series with gaps of one year or more, subsidence rates before and after the gap were analysed separately to ensure similarity.

We used a linear fit to the corrected time series to calculate the mean LOS velocities, assuming that nonlinearities due to seasonal differences or localized disturbance were beyond the scope of this study. We did not analyse temporal dynamics further, as the 46-d repeat of ALOS led to noise, which could be overinterpreted.

As most peat deformation is expected to be vertical, we converted LOS ($d_{LOS}$) into vertical displacement ($d_v$) for every time series using the ALOS incidence angle ($\theta = 34.3°$), $d_v = d_{LOS}/\cos\theta$, and reported all deformation as vertical. Vertical ground displacement is 21% more than LOS displacement; that is, 1 cm of LOS displacement corresponds to 1.2 cm of vertical displacement. We thus multiplied the LOS velocity by a factor of 1.2 to obtain the mean subsidence rate.

To evaluate the role of fire, we compared our InSAR signal with the aggregated dry season (June–October) burned area on peatlands for each year of the time series with the Collection 6 MODIS (Moderate Resolution Imaging Spectroradiometer) Burned Area Product (MCD64monthly). Burned areas were mapped over the time series (Supplementary Fig. 8) and the percentage of each ALOS frame burned each year is shown in Supplementary Table 2.

We find that nearly all fires were excluded from our analysis, and therefore our subsidence measurements and corresponding $CO_2$ emissions estimates reflect C loss from peat oxidation, with a negligible contribution from fires. This is primarily due to the time period of the analysis, rather than a loss of coherence due to fire. We did not capture any major fire events or dry years, with the exception of frame 1 in 2009 (however, no changes in subsidence rate were observed in the frame 1 time series). Additionally, most small fires were excluded from our analysis as they tended to occur in areas with poor coherence (in most cases due to vegetation characteristics). Finally, although 2009 was a major fire year in Central Kalimantan, our time series in this region ended in November 2008, thus excluding these fires (Supplementary Fig. 8i,k and Supplementary Table 2). Likewise, the El Niño dry seasons of 1997 and 2015, when fires were widespread, were not covered by our analysis. Thus, our subsidence measurements mostly reflect carbon losses due to long-term peat oxidation and exclude large-scale peat fires, which are an additional source of regional $CO_2$ emissions in Southeast Asia[46].

Although fire was not included in our analysis, our results indicate that InSAR may have the potential to measure subsidence due to shallow peat fires. The InSAR signal retains coherence in some MODIS burned areas, consistent with our ability to successfully measure subsidence in areas classified as burnt and open land. This is probably because small and medium-sized peat fires, which primarily burn at and just below the peat surface, do not substantially change the character of the land surface. Many peat fires are smouldering, allowing vegetation to survive despite the fire. In contrast, large, deep or intense fires are expected to result in loss of SAR coherence due to changes in the ground texture between repeat satellite passes, but further analysis is needed as no large fires occurred during our observation period.

**Land-use and spatial analysis.** To assess spatial and temporal trends in subsidence rates, we assigned each InSAR pixel a land-use classification on the basis of peatland land-use maps by Miettinen et al.[1]. Land-cover classes for 1990, 2007 and 2015 include pristine peat swamp forest, degraded peat swamp forest (slightly, moderately, heavily), tall shrub/secondary forest, ferns/low shrub, smallholder area, industrial plantations, built-up area and cleared and burnt area. Permanent water, seasonal water and mangrove areas are excluded from our analysis. Full details on land-use classification (derived from 30-m-resolution Landsat data) are available in ref. [1]. These maps were also used to delineate peatland and non-peatland area. Maps of likely oil palm plantation extent for 1990, 2000 and 2007[1,47,48] were used in the space-for-time analysis of ALOS frame 1 data.

*Distance from peat edge.* To analyse spatial variation, we assigned each pixel a distance from the peat edge as a proxy for the distance from the nearest river and peat depth. Coastal peat in Southeast Asia forms in domes separated by rivers, with increasing peat depth further from the river and peat edge. As a digitized map of regional rivers and streams was not available, we use the peat boundaries in ref. [1] for these calculations. We also manually mapped rivers within ALOS frame 1 and found that the same trends hold. Coordinates were projected from WGS84 to UTM 47N for distance calculations.

*Time since drainage.* For our space-for-time substitution analysis on the impact of plantation history on subsidence rates, we used land-use maps developed by Miettinen et al.[1,47,48]. These maps document the extent of plantations (oil palm, acacia and other) on peatlands in 1990, 2000, 2007 and 2010. We selected a site in North Sumatra (frame 1) where oil palm plantations were established at different times across neighbouring peat domes (Fig. 3) and used the time of plantation establishment as a proxy for the time since drainage. To control for previous land use, we selected only land classified as pristine peat swamp forest in 1990. We then selected land which was converted to oil palm plantations in the following time periods: pre-1990, 1990–2000 and 2000–2007 (0–7 years since conversion, 7–17 years since conversion and 17+ years since conversion).

**Regional upscaling.** We used a regression-tree approach to extrapolate the observed 2007–2011 ALOS subsidence values across the region. The regression tree classifies peatland subsidence rates on the basis of 'present' (2007) land-use classification, distance from the edge of the peat and past land-use classification (as a proxy for time since drainage). Subsidence rates for 2015 were then extrapolated across all peatlands in Sumatra and Borneo using 2015 peatland land-use maps[1]. Upscaling relied on 'present' (2015) land-use classification, distance from the edge of the peat and past land-use classification, and subsidence was computed at points on a 1-km grid. Upscaling was limited to Sumatra, Borneo and Peninsular Malaysia, hotspots of land-use change on peatlands. We were unable to calculate projected subsidence rates for the understudied peatlands in Indonesian Papua and Papua New Guinea, as no peatland land-use maps were available there. This regression-tree approach was used to calculate spatially weighted mean subsidence values for the region. Although the mean subsidence and s.e.m. were calculated from an ensemble of regression trees using a bootstrapping approach described below, a single example regional upscaling map is shown to illustrate the method (Extended Data Fig. 3). It is not our intent to make site-specific predictions due to the wide variability in drainage practices.

In combination with the regression-tree approach, we relied on bootstrapping to calculate the regional mean subsidence and the s.e.m. for each land-use class and for the region as a whole. While the s.d. measures the amount of variability in a dataset, the s.e.m. measures how far the sample mean is likely to be from the true mean, and is therefore a more appropriate statistic for regional uncertainty estimates and emissions factors (Table 1). Our bootstrapping analysis sampled the dataset with replacement to create 1,000 synthetic datasets. For each of these synthetic datasets, we calculated a regression tree, and then used this regression tree to calculate gridded subsidence rates across the region and the corresponding regional mean subsidence rates. The distributions of these 1,000 mean subsidence values are shown in Supplementary Fig. 3 and the s.e.m. is calculated as the s.d. of the distribution of the mean. In generating the synthetic datasets, we sampled each InSAR frame, selecting eight frames with replacement for each synthetic dataset. This approach accounts for any potential systematic bias between InSAR frames due to factors such as peat depth, differences in regional drainage policies, high concentrations of certain land uses within a given frame and so on. Due to these frame-correlated factors, frame-based sampling introduced the maximum variability into the synthetic datasets, resulting in the widest range of regression trees and regional mean subsidence rates. It thus provided an upper bound on the s.e.m. and accounted for unquantified variables not directly included in the regression-tree analysis.

We further assessed our regression-tree approach with a cross-validation analysis (Supplementary Table 1). We conducted our cross-validation using two approaches: a standard $k$-fold cross-validation ($k=8$) and a frame-based cross-validation (eight frames). In the first approach, all pixels from the InSAR dataset are randomly divided into eight groups. One group is held out, and a regression tree is fitted to the remaining data and then used to predict the subsidence values of the held-out pixels. Predictions are then compared with the true values. In the second approach, we used a frame-based cross-validation method, in which each frame is held out, and a regression tree is fitted to the remaining seven frames and then used to predict the subsidence values of the held-out frame. Due to systematic differences between frames, this approach resulted in higher variability, and was a more appropriate metric of uncertainty for our dataset, justifying our choice of frame-based bootstrapping to calculate an upper bound on the s.e.m.

**Calculation of $CO_2$ fluxes from subsidence rates.** We calculated $CO_2$ flux from subsidence using a method developed in northern peatlands[49–51] and extended to tropical peat by Couwenberg and Hooijer[9]. During subsidence, peat in the near-surface oxic zone is simultaneously lost to oxidation and compacted, increasing bulk density. In an effort to understand net carbon losses, Couwenberg and Hooijer compared cores extracted from locations where peat had been subject to different histories of land use, drainage and subsidence. They found that profiles of bulk density were nearly identical. As tropical peat subsides, the peat profile remains close to a pseudosteady state; the peat maintains both an oxic surface layer and a deeper anoxic peat column, so the bulk density decrease with depth maintains a similar profile. Only the thickness of the anoxic peat decreases (Extended Data Fig. 5). Thus, the C loss can be calculated from an equivalent loss of deep uncompacted anoxic peat, equal in thickness to the subsidence of the peat surface (Extended Data Fig. 5). Employing this result, regional $CO_2$ emissions were estimated using

$CO_2$ emissions = subsidence
× dry bulk density of deep peat
× carbon concentration of deep peat
× peat area

This approach accounts for both compaction and oxidation of the surface peat but, with an elegant substitution, does not rely on these terms in the equations used to calculate C loss. This approach is well established and has been applied in both northern and tropical peatlands[9,49–51].

We used values from the literature to estimate mean values and uncertainty ranges for peat parameters. We assumed a carbon concentration of 55% (53–57%) and a dry bulk density of 0.08 g cm$^{-3}$ (0.07–0.09 g cm$^{-3}$) on the basis of the review by Couwenberg and Hooijer[9] of subsidence-based carbon loss calculations. These dry bulk density values are consistent with other measurements from the region[52–57], where average values ranged from 0.073 to 0.089 g cm$^{-3}$. Measured values are variable because of small-scale variability, sampling bias due to exclusion of woody material and differences in methodology. Carbon concentrations are less variable, although there is some spatial variability in peat composition. Ombrotrophic fibric and hemic peats have high carbon concentrations while peat soils from mangrove forests and floodplains generally have lower carbon concentrations. This spatial variability is beyond the scope of this upscaling. Additional variability is due to methodology, which includes loss on ignition, wet combustion and elemental analysis. Uncertainties in subsidence ($\delta$subsidence), dry bulk density ($\delta$dry bulk density) and carbon concentration ($\delta$carbon concentration) were propagated to calculate the uncertainty in the total regional $CO_2$ emissions ($\delta CO_2$), assuming that errors in dry bulk density and carbon concentration may be correlated, but are uncorrelated with uncertainty in subsidence, as follows:

$$\delta CO_2 = CO_2 \sqrt{\left(\frac{\delta \text{subsidence}}{\text{subsidence}}\right)^2 + \left(\frac{\delta \text{dry bulk density}}{\text{dry bulk density}} + \frac{\delta \text{carbon concentration}}{\text{carbon concentration}}\right)^2}$$

where '$CO_2$' is the total regional $CO_2$ emissions, on the basis of a peatland area of 15.7 Mha for insular Southeast Asia[1]. Regional emissions factors and uncertainties for each land use (Table 1) were also calculated using the above formulation. In Supplementary Information, we also calculate the $CO_2$ emissions using an older method that relies on shallow, oxic, peat parameters (Extended Data Fig. 5). While this method gives very similar results, these calculated uncertainties are higher because of the uncertainties in both the bulk density of the shallow oxic peat and the estimated fraction of peat lost to oxidation.

## Data availability

The calculated mean subsidence rates that support the findings of this study are archived on Zenodo at https://doi.org/10.5281/zenodo.3694667. The raw SAR data that support the findings of this study are publicly available through the Alaska Satellite Facility data portal at https://vertex.daac.asf.alaska.edu/.

## References


37. Chaussard, E. & Amelung, F. C. Characterization of geological hazards using globally observing spaceborne SAR. *Photogramm. Eng. Remote Sens.* **79**, 982–986 (2013).
38. Chen, C. W. & Zebker, H. A. Phase unwrapping for large SAR interferograms: statistical segmentation and generalized network models. *IEEE Trans. Geosci. Remote Sens.* **40**, 1709–1719 (2002).
39. Elliott, J. R., Biggs, J., Parsons, B. & Wright, T. J. InSAR slip rate determination on the Altyn Tagh Fault, northern Tibet, in the presence of topographically correlated atmospheric delays. *Geophys. Res. Lett.* **35**, L12309 (2008).
40. Chaussard, E., Johnson, C. W., Fattahi, H. & Burgmann, R. Potential and limits of InSAR to characterize interseismic deformation independently of GPS data: application to the southern San Andreas Fault system. *Geochem. Geophys. Geosyst.* **17**, 1214–1229 (2016).
41. Fattahi, H. & Amelung, F. DEM error correction in InSAR time series. *IEEE Trans. Geosci. Remote Sens.* **51**, 4249–4259 (2013).
42. Chaussard, E., Amelung, F. & Aoki, Y. Characterization of open and closed volcanic systems in Indonesia and Mexico using InSAR time series. *J. Geophys. Res. Solid Earth* **118**, 3957–3969 (2013).
43. Zwieback, S., Hensley, S. & Hajnsek, I. Assessment of soil moisture effects on L-band radar interferometry. *Remote Sens. Environ.* **164**, 77–89 (2015).
44. Scott, C. P., Lohman, R. B. & Jordan, T. E. InSAR constraints on soil moisture evolution after the March 2015 extreme precipitation event in Chile. *Sci. Rep.* **7**, 4903 (2017).
45. De Zan, F., Zonno, M. & Lopez-Dekker, P. Phase inconsistencies and multiple scattering in SAR interferometry. *IEEE Trans. Geosci. Remote Sens.* **53**, 6608–6616 (2015).
46. Page, S. E. et al. The amount of carbon released from peat and forest fires in Indonesia during 1997. *Nature* **420**, 61–65 (2002).
47. Miettinen, J., Shi, C., Tan, W. J. & Liew, S. C. 2010 land cover map of insular Southeast Asia in 250-m spatial resolution. *Remote Sens. Lett.* **3**, 11–20 (2012).
48. Miettinen, J. et al. *Historical Analysis and Projection of Oil Palm Plantation Expansion on Peatland in Southeast Asia* (International Council on Clean Transportation, 2012).
49. van den Akker, J. J. H. et al. Emission of $CO_2$ from agricultural peat soils in the Netherlands and ways to limit this emission. In *Proc. 13th International Peat Congress 'After Wise Use—the Future of Peatlands', Vol. 1 Oral Presentations* (eds Farrell, C. & Feehan, J.) 645–648 (International Peat Society, 2008).
50. van den Wyngaert, I. J. J., Kramer, H., Kuikman, P. & Lesschen, J. P. *Greenhouse Gas Reporting of the LULUCF Sector, Revisions and Updates Related to the Dutch NIR 2009* Alterra Report 1035-7 (Alterra, 2009).

51. Leifeld, J., Müller, M. & Fuhrer, J. Peatland subsidence and carbon loss from drained temperate fens. *Soil Use Manag.* **27**, 170–176 (2011).
52. Driessen, P. M. & Rochimah, L. *The Physical Properties of Lowland Peats from Kalimantan (Indonesia)* 56–73 (Soil Research Institute, 1976).
53. Diemont, W. H. & Supardi, M. N. N. Accumulation of organic matter and inorganic constituents in a peat dome in Sumatra, Indonesia. In *International Peat Society Symposium on Tropical Peat and Peatlands for Development* 698–708 (1987).
54. Cameron, C. C., Esterle, J. S. & Palmer, C. A. The geology, botany and chemistry of selected peat-forming environments from temperate and tropical latitudes. *Int. J. Coal Geol.* **12**, 105–156 (1989).
55. Neuzil, S. G. Onset and rate of peat and carbon accumulation in four domed ombrogenous peat deposits, Indonesia. In *Biodiversity and Sustainability of Tropical Peatlands* (eds Rieley, J. O. & Page, S. E.) 55–72 (Samara, 1997).
56. Page, S. E. et al. A record of Late Pleistocene and Holocene carbon accumulation and climate change from an equatorial peat bog (Kalimantan, Indonesia): implications for past, present and future carbon dynamics. *J. Quat. Sci.* **19**, 625–635 (2004).
57. Sumawinata, B., Mulyanto, B., Djajakirana, G. & Pulunggono, H. B. Some considerations of tropical peat for energy. In *Carbon-Climate-Human Interaction on Tropical Peatland: Proc. International Symposium and Workshop on Tropical Peatland* (2007).

## Acknowledgements

We thank D. Sheehan, A. Graham, M. Wrable and J. Murack of the MIT Libraries' GIS and Data Lab for sharing their time, expertise and the computing resources of the Lab. The ALOS-PALSAR data are copyrighted by the Japanese Aerospace Exploration Agency and Ministry of Economy, Trade and Industry and were made available by the US Government Research Consortium through the Alaska Satellite Facility. ISCE is an InSAR processing software package developed at NASA JPL, Caltech and Stanford, which was made available through the Western North America InSAR Consortium. Peatland land-use maps[1] were made available by the Centre for Remote Imaging, Sensing and Processing at the National University of Singapore. This work benefited from access to the University of Oregon high performance computer, Talapas. This research was supported by the National Research Foundation Singapore under its Campus for Research Excellence and Technological Enterprise (CREATE) programme, the Singapore–MIT Alliance for Research and Technology, the US National Science Foundation (grants 1114155, 1114161 and 1923491 to C.F.H.) and the Environmental Solutions Initiative at MIT.

## Author contributions

A.M.H., E.C. and C.F.H. conceived of the study. E.C. and A.M.H. completed InSAR data processing and time-series analysis. A.M.H. and S.S.S. performed land-use and spatial analysis, as well as regional upscaling. A.M.H. wrote the manuscript with contributions from E.C., S.S.S. and C.F.H.

## Competing interests

The authors declare no competing interests.

## Additional information

**Extended data** is available for this paper at https://doi.org/10.1038/s41561-020-0575-4.

**Supplementary information** is available for this paper at https://doi.org/10.1038/s41561-020-0575-4.

**Correspondence and requests for materials** should be addressed to A.M.H.

**Peer review information** Primary Handling Editor: Clare Davis.

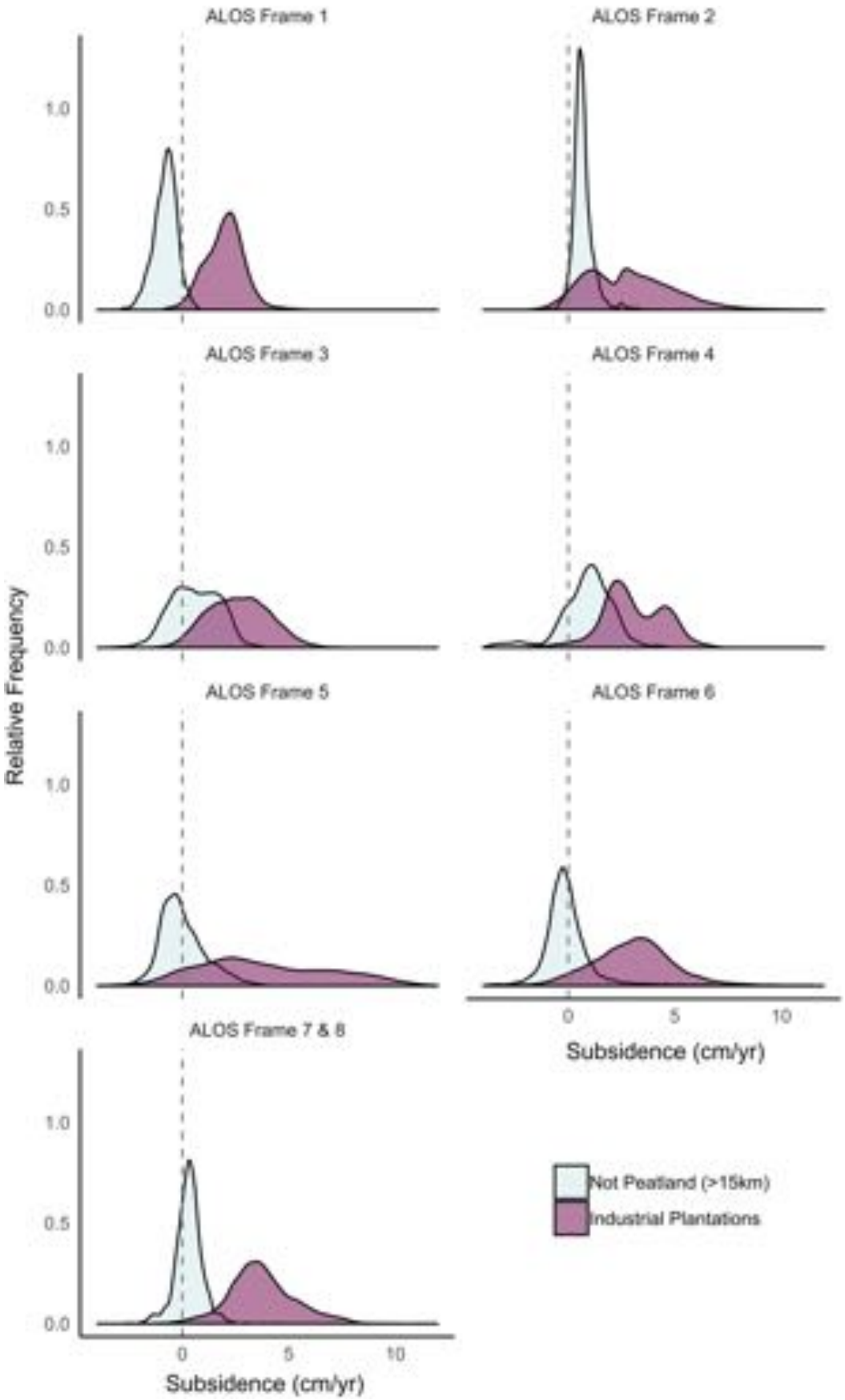


**Extended Data Fig. 1 | Industrial Plantations and Non-Peatland Areas at all Sites.** Density plot of subsidence rates for industrial plantations (2007) and non-peatland areas for each ALOS frame. Non-peatland areas are shown for pixels >15 km from the edge of the peat to exclude transition zones between peatland and mineral soils. Positive values indicate subsidence and negative values indicate uplift.

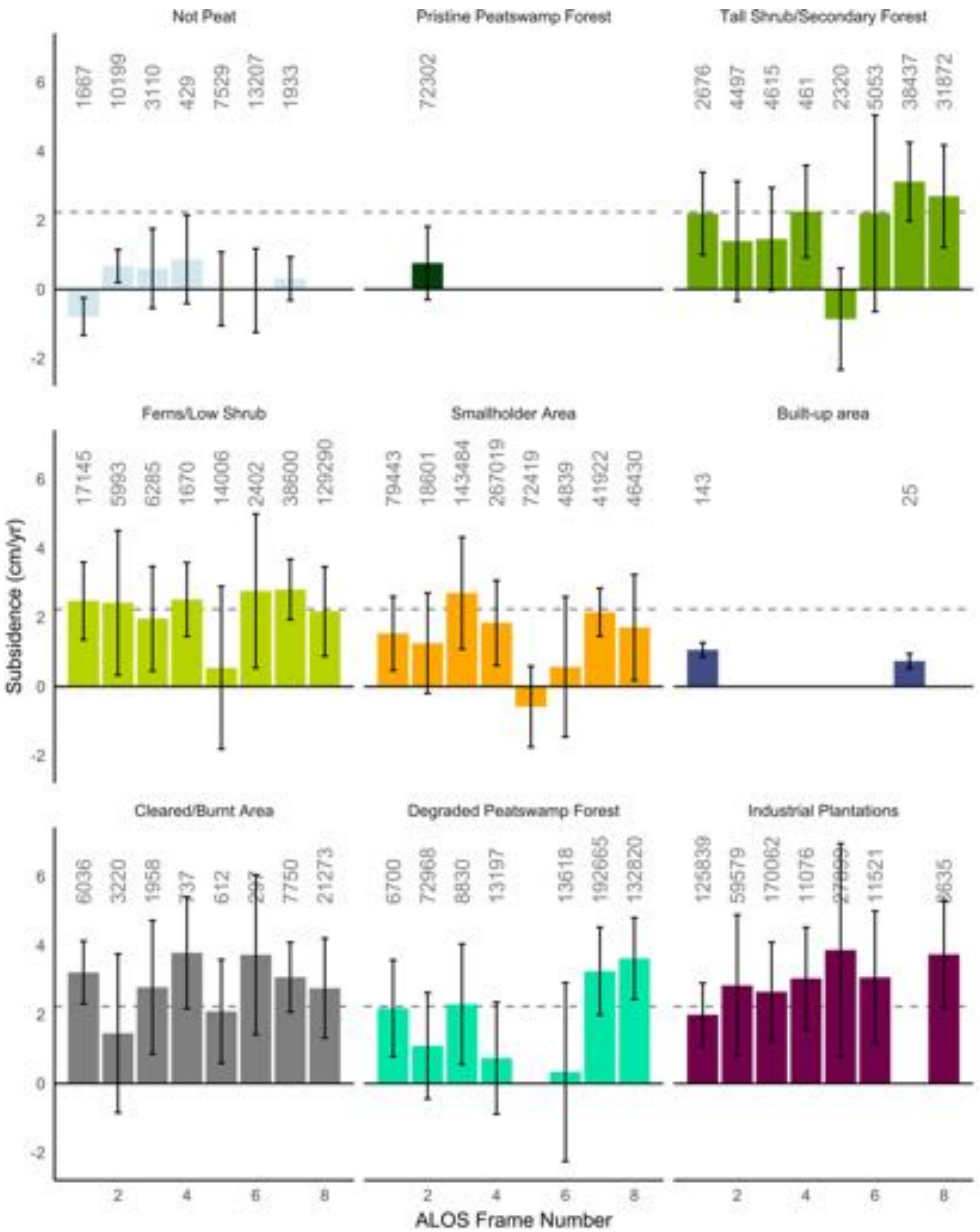


**Extended Data Fig. 2 | Subsidence Rate by Land Use.** Mean subsidence rates (positive values) for each 2007 land use category on peat within each ALOS frame, where available. Numbers indicate number of InSAR measurements averaged for each bar. Dashed lines indicate the mean subsidence rate of 2.24 cm/yr across all peatland measurements. Non-peatland areas (light blue) are shown for pixels >15 km from the edge of the peat to exclude transition zones between peatland and mineral soils. Error bars represent the standard deviation of the data (not the standard error of the mean).

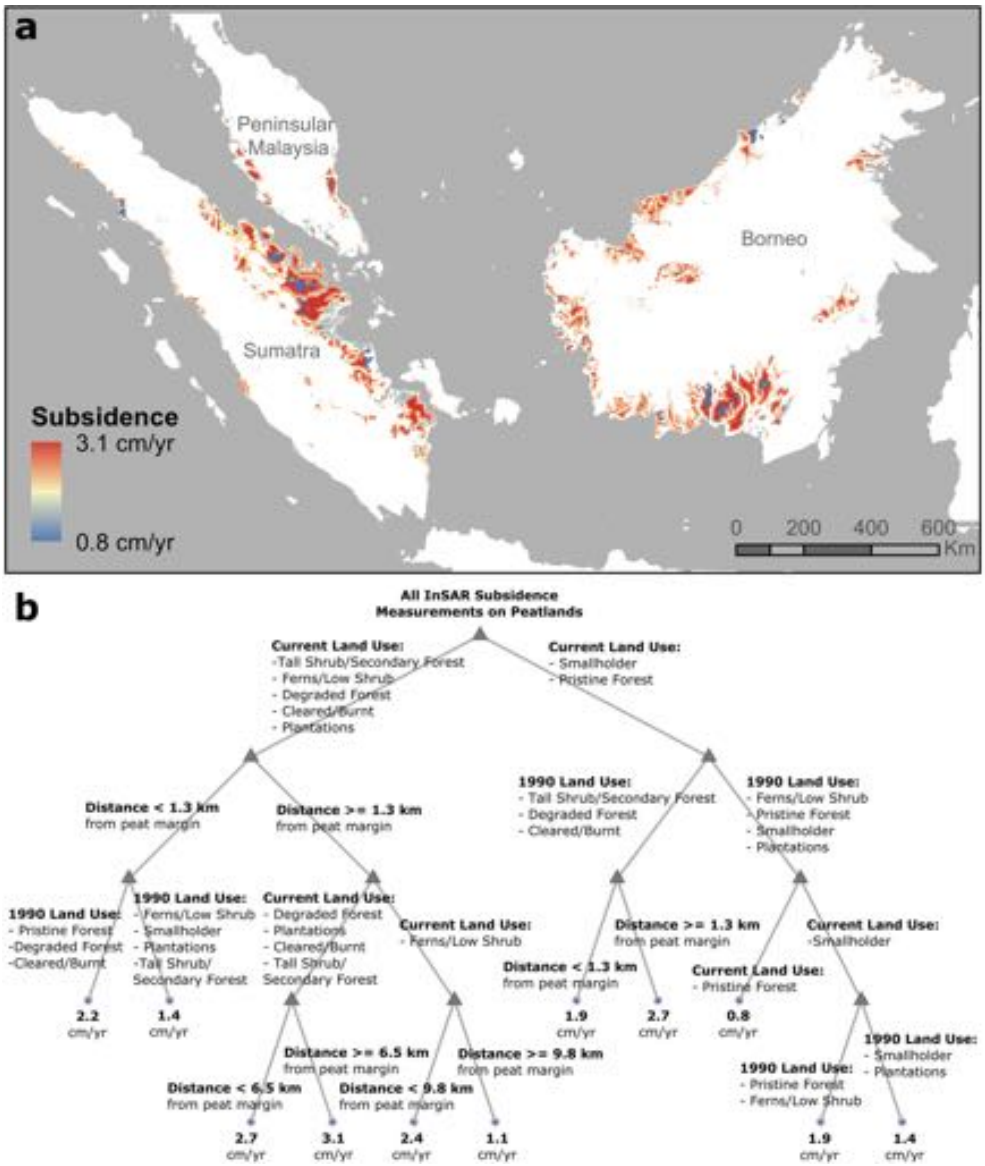


**Extended Data Fig. 3 | Example of Upscaled Subsidence Map and Regression Tree.** (**a**) Map of upscaled subsidence. (**b**) Regression tree schematic. Mean regional subsidence and associated uncertainties were calculated based on a bootstrapping analysis of 1,000 regression trees and corresponding upscaled subsidence maps (Methods). To generate a single regression tree, 2007 land use was used as the *Current Land Use*, concurrent with ALOS measurements from 2007–2011. For regional upscaling, 2015 land use was used as the *Current Land Use*, as the most recently available regional mapping. All land use maps were generated by Miettinen et al.[1]. Total regional $CO_2$ emissions and emissions factors were based on the mean of eight regression trees (each removing data from one ALOS frame). The displayed regression tree, for example purposes only, is based on all data and was used to generate the example regional subsidence map above. The upscaling map is provided as an illustration of the method. It is not our intent to make site-specific predictions due to the wide variability in drainage practices.

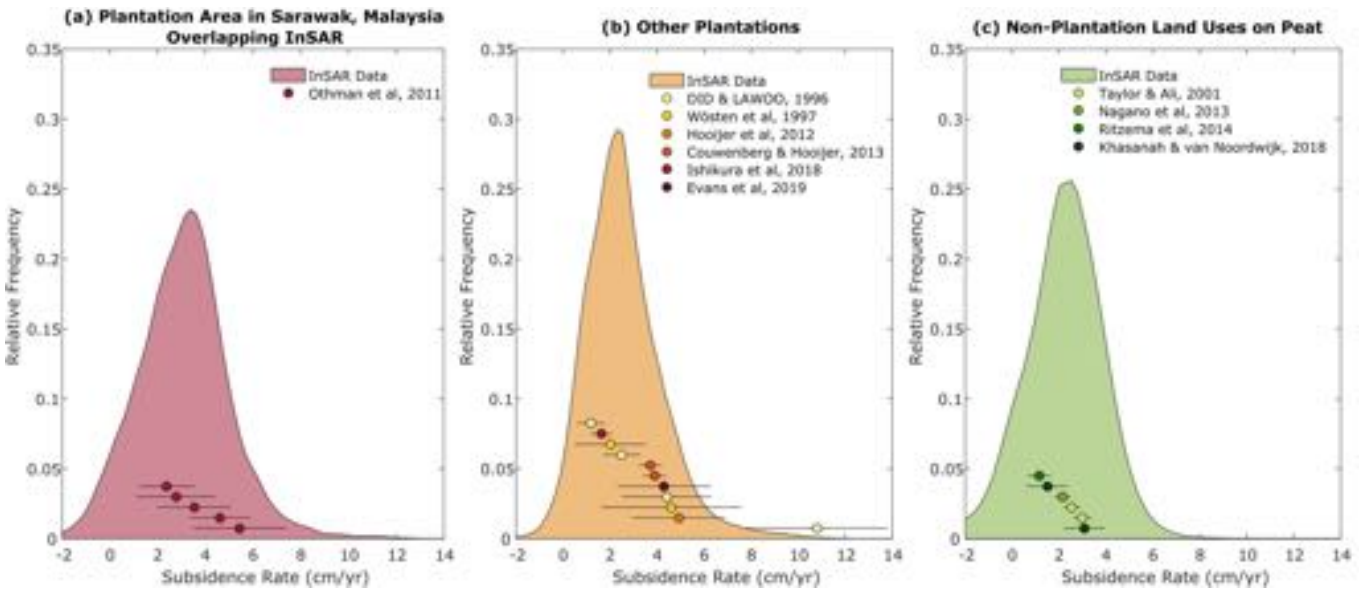


**Extended Data Fig. 4 | InSAR Validation with Ground-Based Subsidence Data.** (**a**) ALOS frame 6 measurements of industrial plantations which overlap in space and time with measurements on oil palm plantations in Sarawak, Malaysia by Othman et al.[8] This is the only area of direct overlap in the region. (**b**) InSAR data from all other industrial plantations compared to ground-based pole measurements also made on plantations, but at different times and/or places. (**c**) InSAR data from all non-plantation land uses on peat (excluding pristine peat swamp forest) compared to ground-based pole measurements made on non-plantation land uses in the region, but at different times and/or places. In all panels, where multiple points are shown from a single study, they represent plantation areas established at different times or distinct land uses with distinct subsidence rates. Error bars indicate the standard deviation of the ground-based measurements within these study groups.

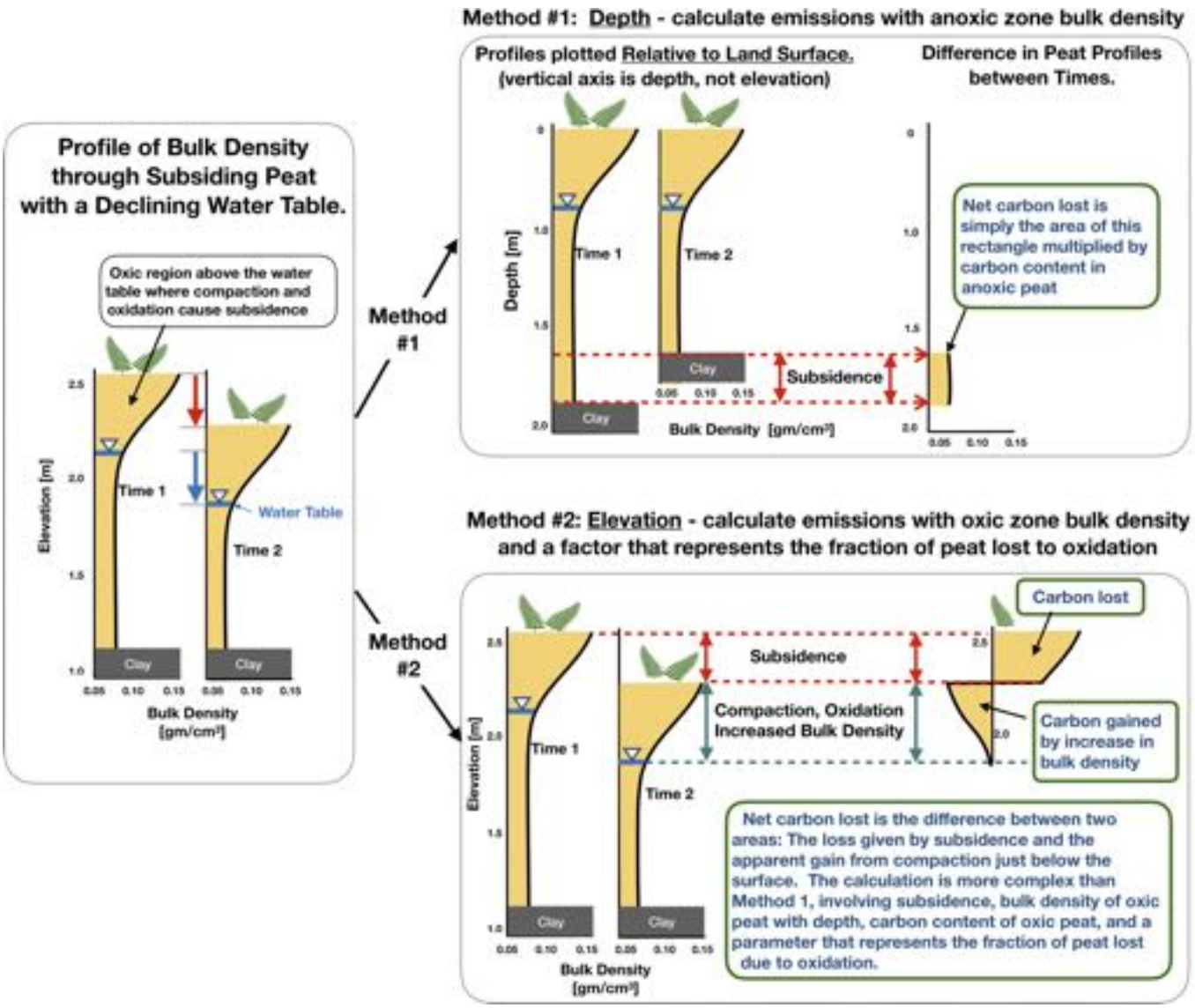


**Extended Data Fig. 5 | Schematic explanation of two methods for calculating carbon loss from bulk density profiles in a subsiding peatland with water table decline.** *Method #1*: The approach first applied to tropical peat by Couwenberg and Hooijier[9]. Bulk density profiles are plotted relative to the land surface, which has subsided. It is evident from these bulk density profiles, before and after subsidence, that the carbon loss can be calculated from the change in thickness of the anoxic peat, the small yellow rectangle on the far right. *Method #2*: Bulk density profiles are plotted relative to elevation. The net carbon lost must be the same regardless of how the plot is constructed, but the calculation is more complex for Method #2. Here the net carbon lost is shown as loss in carbon due to the drop in the land surface, minus the apparent gain in carbon from the increased bulk density below the elevation that is now the land surface. The carbon lost is the difference between the gain and loss shown by the yellow regions on the far right. Our results rely on Method #1. However, calculations of $CO_2$ emissions from Method #2 yield similar results with higher uncertainties. Assuming a dry bulk density of $0.11 \pm .03$ g/cm$^3$ and carbon content of $55 \pm 2$ % in the compacted oxic peat, a mean subsidence rate of $2.24 \pm 0.23$ cm/yr, a peat area of 15.7 Mha, and the fraction of subsidence due to compaction of $75 \pm 15$ % as found by Hooijer et al.[2], we calculate $CO_2$ emissions equivalent to $160 \pm 61$ MtC/yr (compared to $155 \pm 30$ MtC/yr using Method #1).

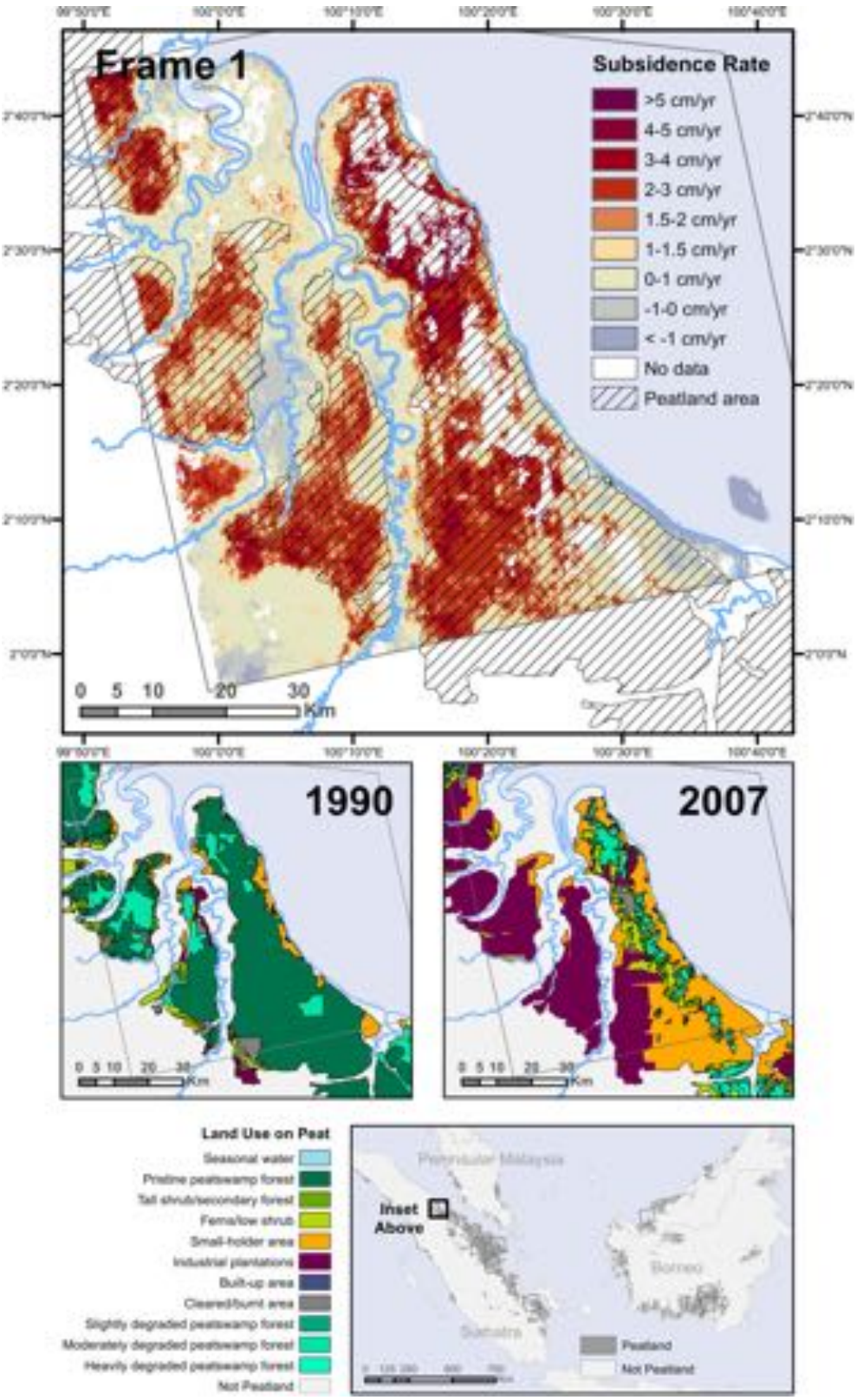


**Extended Data Fig. 6 | Frame 1 Subsidence and Land Use Map.** ALOS Frame 1 mean subsidence rates (top), 1990 land use (left) and 2007 land use (right). Positive values indicate subsidence and negative values indicate uplift. Peatland extent and land-use maps adapted with permission from ref. [1], Elsevier.

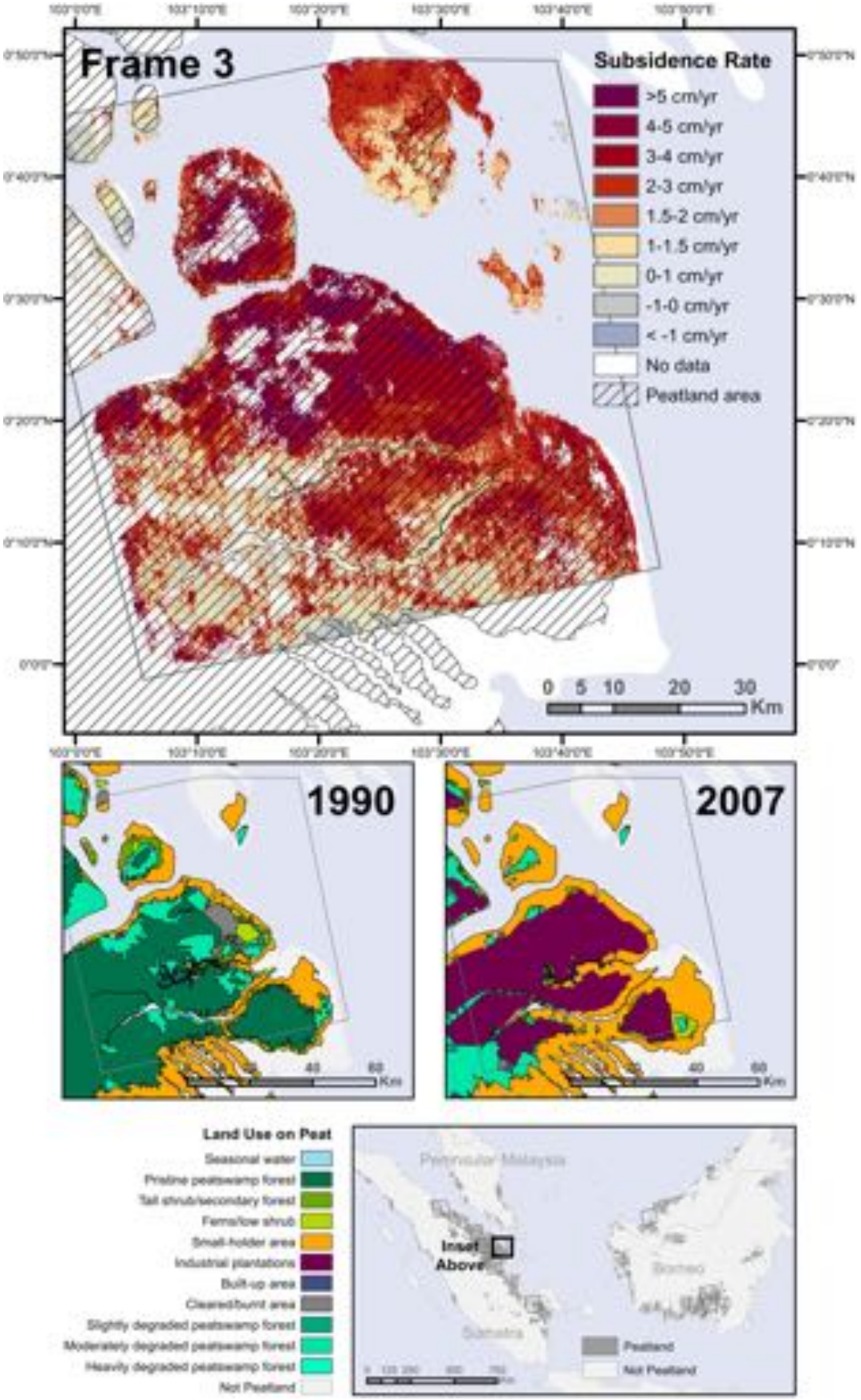


**Extended Data Fig. 7 | Frame 3 Subsidence and Land Use Map.** ALOS Frame 3 mean subsidence rates (top), 1990 land use (left) and 2007 land use (right). Positive values indicate subsidence and negative values indicate uplift. Peatland extent and land-use maps adapted with permission from ref. [1], Elsevier.

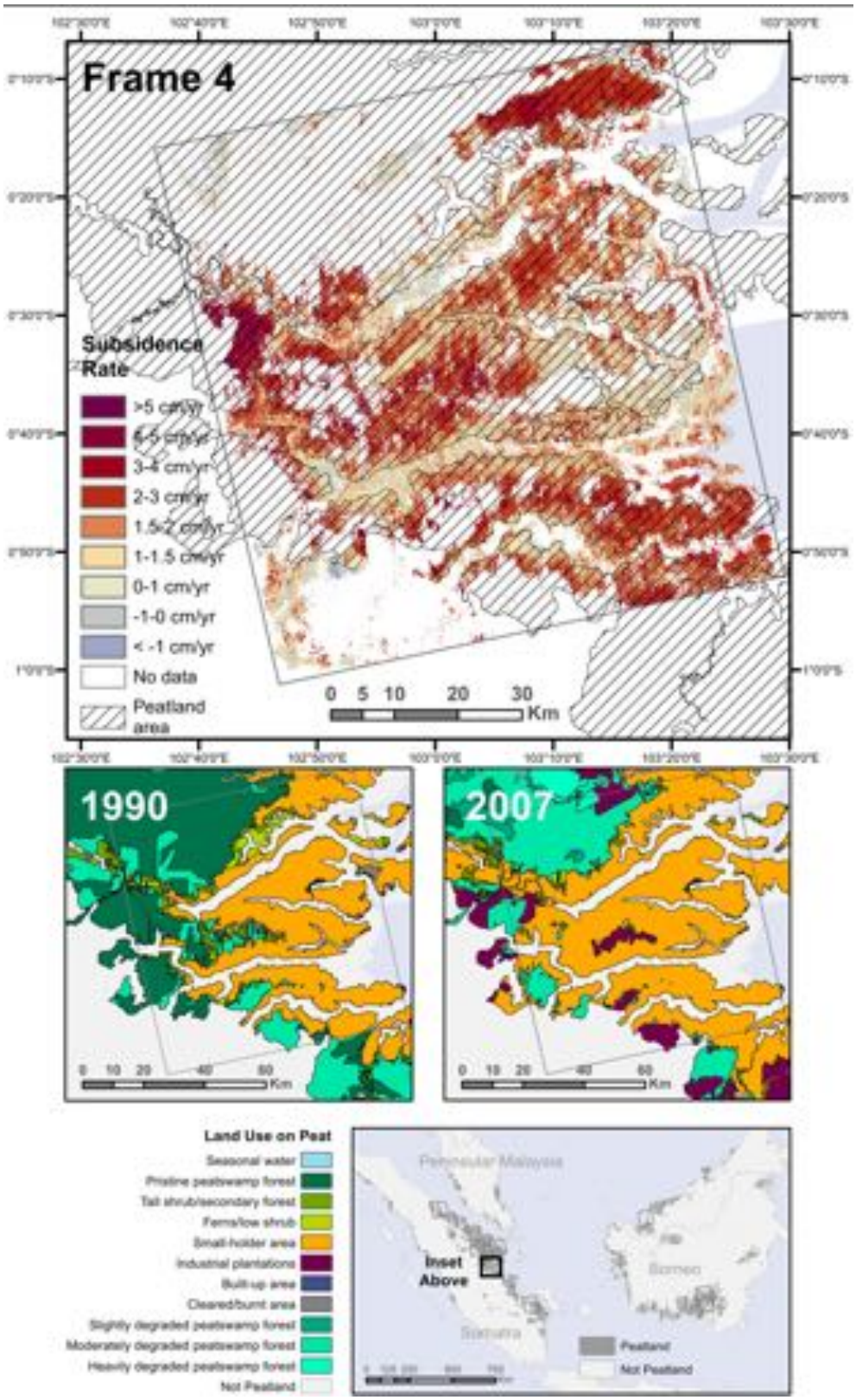


**Extended Data Fig. 8 | Frame 4 Subsidence and Land Use Map.** ALOS Frame 4 mean subsidence rates (top), 1990 land use (left) and 2007 land use (right). Positive values indicate subsidence and negative values indicate uplift. Peatland extent and land-use maps adapted with permission from ref. [1], Elsevier.

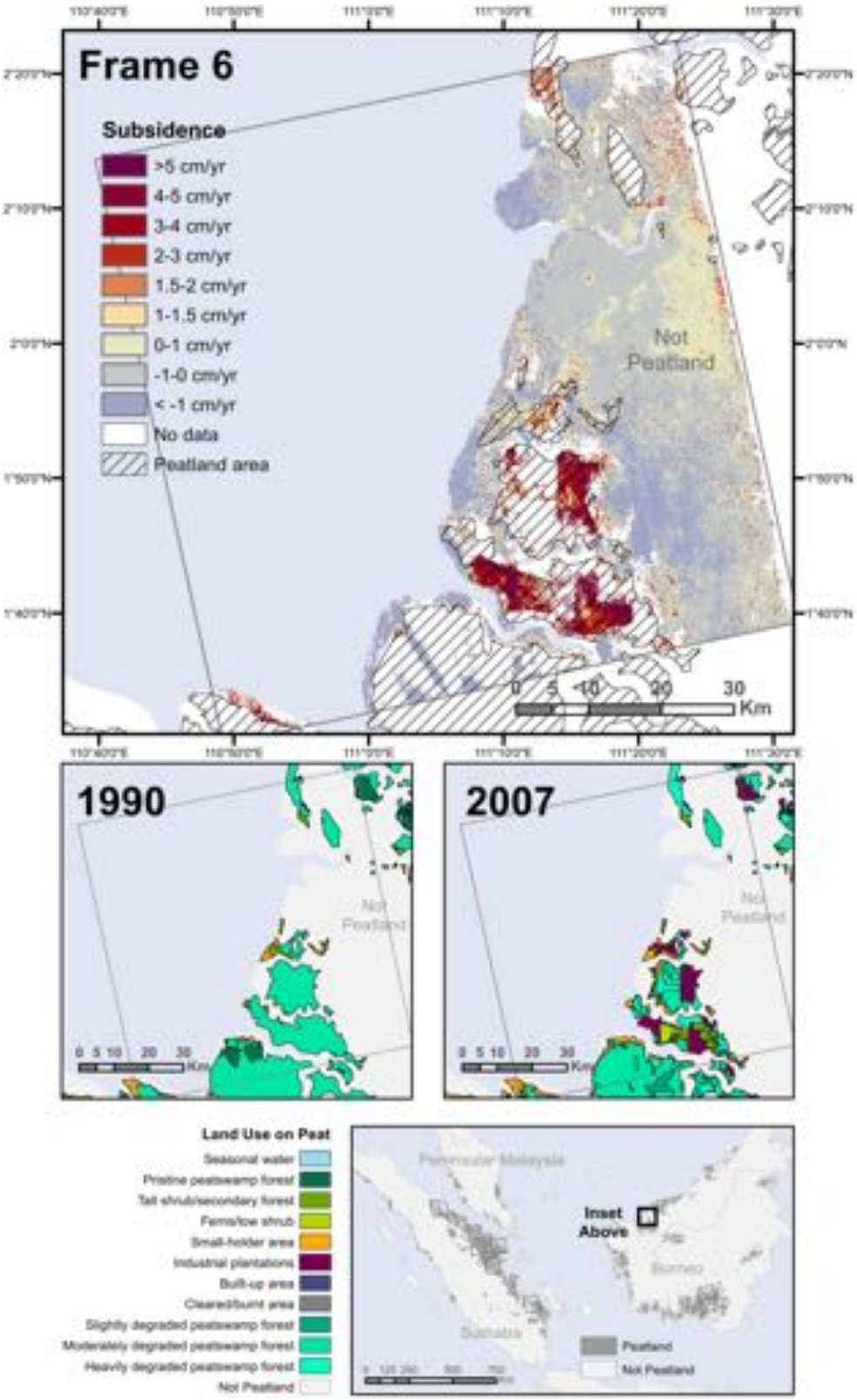


**Extended Data Fig. 9 | Frame 6 Subsidence and Land Use Map.** ALOS Frame 6 mean subsidence rates (top), 1990 land use (left) and 2007 land use (right). Positive values indicate subsidence and negative values indicate uplift. Peatland extent and land-use maps adapted with permission from ref. [1], Elsevier.

**Extended Data Table 1 | Study sites (ALOS frames) listed from north to south, first in Sumatra, then in Borneo**

| Frame | Province (Island) | Dominant Land Use | Peatland Area (Total Area) Surveyed | Additional Information | Time Range and InSAR Acquisition Dates Removed (mm/dd/yy; notes) |
|---|---|---|---|---|---|
| 1 | North Sumatra (Sumatra) | Oil Palm | 0.25 Mha (0.43 Mha) | Plantations established at different times | 07/03/07 – 02/23/10 10/05/08, 10/08/09, 01/08/10 (atm. noise and uplift) |
| 2 | Riau (Sumatra) | Acacia, Degraded peat swamp forest | 0.51 Mha (0.66 Mha) | Subsidence poles: Hooijer et. al. (2012) | 06/28/07 – 11/21/10 09/30/2008 (ionospheric noise) 2-part analysis for 1.5yr gap; eliminates clear incidences of phase unwrapping error |
| 3 | Riau (Sumatra) | Oil Palm | 0.38 Mha (0.43 Mha) | | 11/25/07 – 12/03/10 01/10/08, 10/12/08 (atm. noise), 12/03/10 (uplift) |
| 4 | Riau (Sumatra) | Smallholder | 0.48 Mha (0.68 Mha) | | 07/27/07 – 09/19/10 06/19/10, 08/04/10, 09/19/10 (remove points after 1yr gap because beginning of timeseries is alone sufficient to yield clear subsidence signal) |
| 5 | South Sumatra (Sumatra) | Smallholder, Acacia | 0.26 Mha (0.55 Mha) | | 07/22/07 – 01/24/09 Maintained all points. |
| 6 | Sarawak (Borneo) | Oil Palm | 0.08 Mha (0.29 Mha) | Subsidence poles: Othman et. al. (2011) | 01/28/07 – 08/05/09 03/17/08, 06/17/08, 06/20/09 (tropospheric noise) |
| 7 | Central Kalimantan (Borneo) | Degraded peat swamp forest | 0.34 Mha (0.61 Mha) | Overlaps well-studied Ex-Mega Rice Project area | 02/21/07 – 11/26/08 10/09/07, 10/11/08 (analyzed with site 8) |
| 8 | Central Kalimantan (Borneo) | Degraded peat swamp forest | 0.41 Mha (0.62 Mha) | Overlaps well-studied Ex-Mega Rice Project area | 02/21/07 – 11/26/08 10/09/07, 10/11/08 (analyzed with site 7) |
| 9 | Jambi (Sumatra) | Oil Palm | | Subsidence poles: Hooijer *et al.* (2012), Couwenberg & Hooijer (2013) | 11/25/07 – 12/03/10 Site removed. Insufficient time points and two-year gap in timeseries. |
| | | Total Peatland Area: Total Land Area: | 2.7 Mha 4.29 Mha | | |

Frame 9 is listed last as it is not included in the subsequent analysis.